JOURNAL OF THE AMERICAN CHEMICAL SOCIETY

Article

(EDT-TTF-CONH)[ReSe(CN)], a Metallic Kagome-Type Organic–Inorganic Hybrid Compound: Electronic Instability, Molecular Motion, and Charge Localization

Stphane A. Baudron, Patrick Batail, Claude Coulon, Rodolphe Clrac, Enric Canadell, Vladimir Laukhin, Roberto Melzi, Pawel Wzietek, Denis Jrome, Pascale Auban-Senzier, and Sylvain Ravy

J. Am. Chem. Soc., **2005**, 127 (33), 11785-11797• DOI: 10.1021/ja0523385 • Publication Date (Web): 29 July 2005

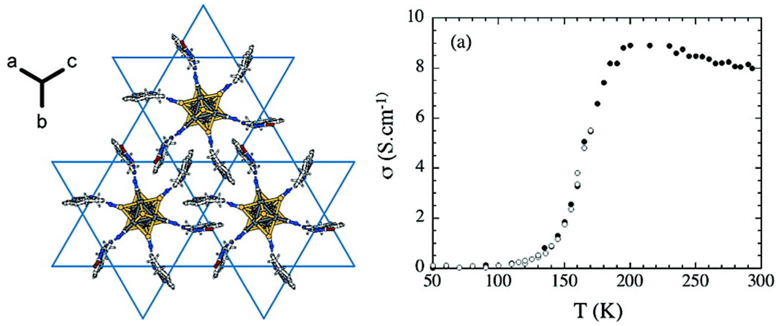

ACS Publications
High quality. High impact.

Journal of the American Chemical Society is published by the American Chemical Society. 1155 Sixteenth Street N.W., Washington, DC 20036

J|A|C|S
ARTICLES

$(EDT\text{-}TTF\text{-}CONH_2)_6[Re_6Se_8(CN)_6]$, a Metallic Kagome-Type Organic−Inorganic Hybrid Compound: Electronic Instability, Molecular Motion, and Charge Localization

Stéphane A. Baudron,[†] Patrick Batail,*[,†] Claude Coulon,*[,‡] Rodolphe Clérac,[‡]
Enric Canadell,[§] Vladimir Laukhin,[§,#] Roberto Melzi,[||] Pawel Wzietek,[||]
Denis Jérome,[||] Pascale Auban-Senzier,[||] and Sylvain Ravy[||]

Contribution from the Laboratoire de Chimie, Ingénierie Moléculaire et Matériaux d'Angers, UMR 6200 CNRS-Université d'Angers, 2 Boulevard Lavoisier, 49045 Angers, France, Centre de Recherches Paul Pascal (CRPP-CNRS, UPR 8641), 115 Avenue Dr. Schweitzer, 33600 Pessac, France, Institut de Ciència de Materials de Barcelona (ICMAB-CSIC), Campus de la UAB, E-08193 Bellaterra, Spain, Institució Catalana de Recerca i Estudis Avançats (ICREA), 08010 Barcelona, Spain, and Laboratoire de Physique des Solides, UMR 8502 CNRS-Université de Paris-Sud, 91405 Orsay, France

Received April 11, 2005; E-mail: patrick.batail@univ-angers.fr

---

Abstract: $(EDT\text{-}TTF\text{-}CONH_2)_6[Re_6Se_8(CN)_6]$, space group $R\bar{3}$, was prepared by electrocrystallization from the primary amide-functionalized ethylenedithiotetrathiafulvalene, EDT-TTF-$CONH_2$ ($E_{1/2}{}^1 = 0.49$ V vs SCE in CH_3CN), and the molecular cluster tetraanion, $[Re_6Se_8(CN)_6]^{4-}$ ($E_{1/2} = 0.33$ V vs SCE in CH_3CN), equipped with hydrogen bond donor and hydrogen bond acceptor functionalities, respectively. Its Kagome topology is unprecedented for any TTF-based materials. The metallic state observed at room temperature has a strong two-dimensional character, in coherence with the Kagome lattice symmetry, and the presence of minute amounts of $[Re_6Se_8(CN)_6]^{(3-)\bullet}$ identified by electron spin spectroscopy. A structural instability toward a distorted form of the Kagome topology of lesser symmetry is observed at ca. 180 K. The low-temperature structure is associated with a localized, electrically insulating electronic ground state and its magnetic susceptibility accounted for by a model of uniform chains of localized $S = {}^1/_2$ spins in agreement with the 100 K triclinic crystal structure and band structure calculations. A sliding motion, within one out of the three $(EDT\text{-}TTF\text{-}CONH_2)_2$ dimers coupled to the $[Re_6Se_8(CN_6)^{(3-)\bullet}]/[Re_6Se_8(CN_6)^{4-}]$ proportion at any temperature, and the electronic ground state of the organic−inorganic hybrid material are analyzed on the basis of ESR, dc conductivity, ^1H spin−lattice relaxation, and static susceptibility data which qualify a Mott localization in $[EDT\text{-}TTF\text{-}CONH_2]_6[Re_6Se_8(CN)_6]$. The coupling between the metal−insulator transition and a structural transition allows for the lifting of a degeneracy due to the ternary axis in the high temperature, strongly correlated metallic phase which, in turn, leads to Heisenberg chains at low temperature.

Introduction

The Kagome topology is a planar, hexagonal net comprising triangles and hexagons.[1−4] When unpaired spins are localized at the triangular corners, the prediction that these systems are susceptible to exhibit a manifold of low-energy excitations directing diverse magnetic ground states generates an intense interest, especially for $S = {}^1/_2$ spins.[5] Despite recent advances,[2−4,6,7] there are only few systems available today, among which the molecular salt (*m*-MPYNN)X (*m*-MPYNN is *m*-*N*-methylpyridinium and X = I^-, BF_4^-, ClO_4^-, etc.), a Kagome antiferromagnet where the unpaired ($S = {}^1/_2$) spin of any nitronylnitroxide radical is ferromagnetically coupled within molecular ($S = 1$) dimers.[8]

The chemistry reported here relies on the construction of functional, long-range ordered cation−anion interfaces[9] by directing hydrogen or halogen bonding interactions and express-

---

[†] UMR 6200, CNRS-Université d'Angers.

[‡] Centre de Recherches Paul Pascal, Pessac.

[§] ICMAB-CSIC, Bellaterra.

[#] ICREA, Barcelona.

[||] UMR 8502 CNRS-Université Paris-Sud, Orsay.

(1) Johnston, R. L.; Hoffmann, R. *Polyhedron* **1990**, *9*, 1901.

(2) Vander Griend, D. A.; Boudin, S.; Caignaert, V.; Poeppelmeier, K. R.; Wang, Y.; Dravid, V. P.; Azuma, M.; Takano, M.; Hu, Z.; Jorgensen, J. D. *J. Am. Chem. Soc.* **1999**, *121*, 4787.

(3) (a) Grohol, D.; Papoutsakis, D.; Nocera, D. G. *Angew. Chem., Int. Ed.* **2001**, *40*, 1519. (b) Grohol, D.; Nocera, D. G. *J. Am. Chem. Soc.* **2002**, *124*, 2640. (c) Papoutsakis, D.; Grohol, D.; Nocera, D. G. *J. Am. Chem. Soc.* **2002**, *124*, 2647. (d) Nocera, D. G.; Bartlett, B. M.; Grohol, D.; Papoutsakis, D.; Shores, M. P. *Chem. Eur. J.* **2004**, *10*, 3850.

(4) (a) Paul, G.; Choudhury, A.; Rao, C. N. R. *Chem. Commun.* **2002**, 1904. (b) Behera, J. N.; Paul, G.; Choudhury, A.; Rao, C. N. R. *Chem. Commun.* **2004**, 456.

(5) (a) Mila, F. *Phys. Rev. Lett.* **1998**, *81*, 2356. (b) Mila, F.; Dean, D. *Eur. Phys. J. B* **2002**, *26*, 301.

(6) Greedan, J. E. *J. Mater. Chem.* **2001**, *11*, 37.

(7) (a) Moulton, B.; Lu, J.; Hajndl, R.; Hariharan, S.; Zaworotko, M. J. *Angew. Chem., Intl. Ed.* **2002**, *41*, 2821. (b) Atwood, J. L. *Nat. Mater.* **2002**, *1*, 91.

(8) (a) Awaga, K.; Inabe, T.; Nakamura, T.; Matsumoto, M.; Maruyama, Y. *Chem. Phys. Lett.* **1992**, *195*, 21. (b) Awaga, K.; Okuno, T.; Yamagushi, A.; Hasegawa, M.; Inabe, T.; Maruyama, Y.; Wada, N. *Phys. Rev.* **1994**, *B49*, 3975.

(9) Heuzé, K.; Fourmigué, M.; Batail, P.; Canadell, E.; Auban-Senzier, P. *Chem. Eur. J.* **1999**, *5*, 2971.

10.1021/ja0523385 CCC: $30.25 © 2005 American Chemical Society

ing the symmetry of the molecular precursors all the way up to the scale of bulk crystalline assemblages.[10] These principles govern the deliberate association by electrocrystallization of the primary amide-functionalized ethylenedithiotetrathiafulvalene, EDT-TTF-CONH$_2$ ($E_{1/2}{}^1 = 0.49$ V vs SCE in CH$_3$CN)[11] and the molecular cluster tetraanion, $[Re_6Se_8(CN)_6]^{4-}$ ($E_{1/2} = 0.33$ V vs SCE in CH$_3$CN),[12] equipped with hydrogen bond donor and hydrogen bond acceptor functionalities, respectively. Such organic−inorganic hybrid combinations, in particular those involving inorganic clusters[13,14] and extended inorganic networks,[14] are proving their interest in the field of molecular conductors[15] as they are delivering fascinating architectures associated with singular physical properties or combination of properties.

Thus, we report the synthesis, crystal structures, and electronic band structure calculations, integrated with in-depth electron spin resonance and static susceptibility, dc conductivity, and ^{1}H spin−lattice relaxation studies of (EDT-TTF-CONH$_2$)$_6$[Re$_6$Se$_8$(CN)$_6$] whose Kagome topology is unprecedented for any TTF-based materials. The metallic state observed at room temperature has a strong two-dimensional character, in coherence with the Kagome lattice symmetry and the presence of minute amounts of $[Re_6Se_8(CN)_6]^{(3-)\bullet}$,[16] identified by electron spin spectroscopy at room temperature. A structural instability toward a distorted form of the Kagome topology of lesser symmetry is observed at ca. 180 K. The low-temperature structure is associated with a localized, electrically insulating electronic ground state where the cluster sites are now populated by the 24-electron, diamagnetic cluster tetraanion, $[Re_6Se_8(CN)_6]^{4-}$ only, while its magnetic susceptibility is successfully accounted for by a model of uniform chains of localized $S = {}^1/_2$ spins in agreement with the averaged 100 K crystal structure, band structure calculations, ESR, static susceptibility, and ^{1}H spin−lattice relaxation investigations.

Experimental Section

Preparation of (EDT-TTF-CONH$_2$)$_6$[Re$_6$Se$_8$(CN)$_6$]. EDT-TTF-CONH$_2$[11] (5 mg) was oxidized in the presence of (PPh$_4$)$_4$[Re$_6$Se$_8$(CN)$_6$][12] (25 mg) in a 1/1 mixture of freshly distilled acetonitrile and tetrahydrofuran (12 mL). Electrocrystallization experiments[17] carried out in two-compartment cells with platinum wires ($l = 2$ cm, Ø = 1 mm) at a constant current (0.5 μA) at 25 °C yield octahedral black crystals.

Single-Crystal X-ray Diffraction. Data were collected on an imaging plate diffraction system (IPDS-Stoe).[18] The structures were solved by direct methods and refined against F^2 using SHELXL-97. All non-hydrogen atoms were refined anisotropically; the H atoms were introduced at calculated positions and not refined. In the crystal structure at 293 K, one carbon atom of the ethylenedithio bridge is disordered over two positions, and consequently, the hydrogen atoms on this carbon have not been introduced.

Unit-cell parameters were determined on a single crystal at several low temperatures down to 200 K using an ENRAF-NONIUS Mach III four-circles diffractometer. Below 200 K, the intensities of the Bragg reflections decrease dramatically as the Bragg peaks experience an apparent broadening up to the point where the determination of the unit cell parameter is severely hampered. Bragg peaks are eventually recovered gradually below 150 K; a data set was then collected at 100 K on a STOE-IPDS diffractometer from which a satisfactory average structure solution was obtained and refined (Table S1, Supporting Information). In that case, the H atoms were introduced, and only the Re, Se, and S atoms were refined anisotropically. Note that the considerable increase of the mosaicity across the transition of an otherwise high-quality single crystal is fully reversible as sharp, narrow Bragg peaks are recovered upon bringing the crystal back to room temperature. However, the data and structure refinement at 100 K are of lesser quality than those of the room-temperature structure. Several atoms show disorder and have thus been refined with isotropic thermal parameters only, and the hydrogen atoms have not been introduced on these atoms. Details of crystallographic data and structure refinement are given in the Supporting Information.

Band Structure Calculations. The tight-binding calculations used an extended Hückel-type Hamiltonian.[19] The off-diagonal matrix elements of the Hamiltonian were calculated according to the modified Wolfsberg−Helmholz formula.[20] A basis set composed of double-ζ Slater-type orbitals for C, N, O, and S and single-ζ Slater-type orbitals for H was used. The exponents, contraction coefficients, and atomic parameters were taken from previous work.[21]

Magnetic Measurements. Magnetic susceptibility measurements were performed on a polycrystalline sample with a Quantum Design MPMS-XL SQUID magnetometer in the temperature range of 1.8−350 K and up to 50 kOe. Experimental data were also corrected for the sample holder and for the diamagnetic contribution calculated from Pascal constants. ESR spectra were recorded on an oriented single crystal on an X band (9.3 GHz) Bruker ESP300E spectrometer equipped with an ESR900 cryostat (3.8−300 K) from Oxford Instruments. The ESR conductivity was deduced from the line asymmetry using the data of Pifer and Magno.[22] These authors give the relationship between the dimensionless parameter $\lambda = d/\delta$ (where d is the sample thickness and δ is the skin depth) and the electrical conductivity for isotropic films. For moderate line asymmetries (A/B < 2.5), we have checked that the simple expression: $\lambda^2 = -3.54 + 4.78x - 1.44x^2 + 0.2x^3$ (where x = A/B) reproduces these data. We have used this expression to deduce the electrical conductivity in the isotropic (111) plane.

Results and Discussion

Hydrogen-Bonded $\bar{3}$ Symmetry Motifs and Tubules and Their Auto-Assembly into a Kagome Topology. The bulk, truncated octahedral black crystals belong to the rhombohedral system, space group $R\bar{3}$ (Table S1, Supporting Information) in which the octahedral cluster anion resides on a $\bar{3}$ symmetry site with one EDT-TTF-CONH$_2$ in general position. As exemplified in Figure 1, within any hybrid (111) layer the organic radical cations and mineral cluster anions are neatly intertwined to satisfy the $\bar{3}$ symmetry. Each cluster anion is surrounded by six centrosymmetrical dimers. Hence, the slab is deciphered as the augmented, molecular Kagome-type topology drawn in Figure 1 where (EDT-TTF-CONH$_2$)$_2$ dimers are located at each corner of the triangles and [Re$_6$Se$_8$(CN$_6$)] cluster anions fill the hexagonal voids. As expected, one hydrogen of the amide group

---

[10] Fourmigué, M.; Batail, P. *Chem. Rev.* **2004**, *104*, 5379.
[11] Heuzé, K.; Fourmigué, M.; Batail, P. *J. Mater. Chem.* **1999**, *9*, 2373.
[12] Yoshimura, T.; Ishizaka, S.; Sasaki, Y.; Kim, H.-B.; Kitamura, N.; Naumov, N. G.; Sokolov, M. N.; Fedorov, V. E. *Chem. Lett.* **1999**, 1121.
[13] Gabriel, J.-C.; Boubekeur, K.; Uriel, S.; Batail, P. *Chem. Rev.* **2001**, *101*, 2037.
[14] Coronado, E.; Day, P. *Chem. Rev.* **2004**, *104*, 5419.
[15] Batail, P. *Chem. Rev.* **2004**, *104*, 4887.
[16] (a) Bennett, M. V.; Shores, M. P.; Beauvais, L. G.; Long, J. R. *J. Am. Chem. Soc.* **2000**, *122*, 6664. (b) Naumov, N. G.; Ostanina, E. V.; Virovets, A. V.; Schmidtman, M.; Müller, A.; Fedorov, V. E. *Russ. Chem. Bull.* **2002**, *51*, 866. (c) Baudron, S. A.; Deluzet, A.; Boubekeur, K.; Batail, P. *Chem. Commun.* 2002, 2124.
[17] Batail, P.; Boubekeur, K.; Fourmigué, M.; Gabriel, J.-C. *Chem. Mater.* **1998**, *10*, 3005.
[18] Stoe-IPDS Software manual V2.87, December 1997, STOE, Darmstadt, Germany.
[19] Whangbo, M.-H.; Hoffmann, R. *J. Am. Chem. Soc.* **1978**, *100*, 6093.
[20] Ammeter, J.; Bürgi, H.-B.; Thibeault, J.; Hoffmann, R. *J. Am. Chem. Soc.* **1978**, *100*, 3686.
[21] Heuzé, K.; Fourmigué, M.; Batail, P.; Coulon, C.; Clérac, R.; Canadell, E.; Auban-Senzier, P.; Ravy, S.; Jérome, D. *Adv. Mater.* **2003**, *15*, 1251.
[22] Pifer, J. H.; Magno, R. *Phys. Rev. B* **1971**, *3*, 663.

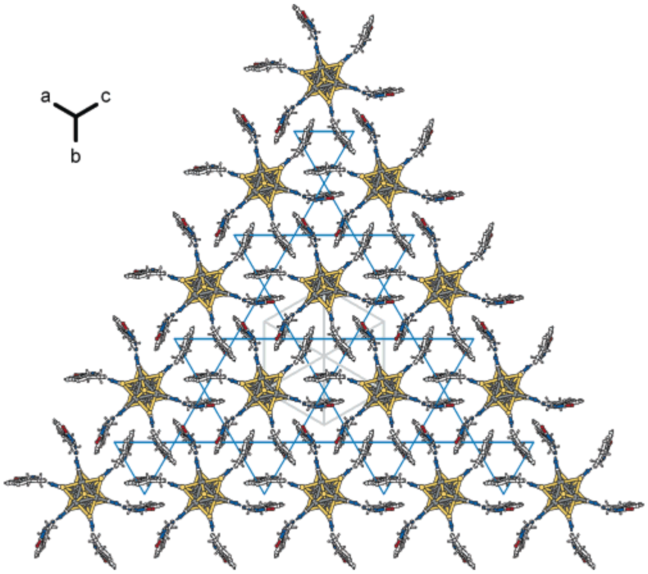

Figure 1. This projection of one single hybrid slab down [111] illustrates how any hydrogen-bonded, molecular motif of $\bar{3}$ symmetry formulated, [EDT-TTF-CONH$_2$]$_6$[Re$_6$Se$_8$(CN)$_6$] (also shown in Figure 2) clicks into six of its congeners to build an extended two-dimensional array of an unprecedented kind. Notice the subsequent sets of six equivalent mixed valence dimers surrounding any cluster core. The blue lines connecting the centers of [EDT-TTF-CONH$_2$]$_2$ dimers materialize the Kagome lattice.

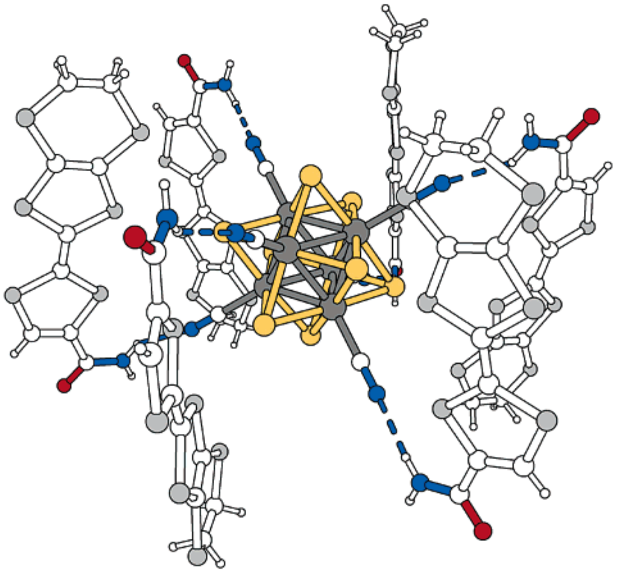

Figure 2. A perspective view of the $\bar{3}$ symmetry motif assembled via one single N−H···N≡C hydrogen bond (H···N, 2.279 Å; ∠N−H···N, 147.6°).

attached to the π-donor is engaged in a robust N−H···N≡C hydrogen bond (H···N, 2.279 Å, ∠N−H···N, 147.6°)[10] with each cluster cyanide acceptor to yield the compound 6:1 stoichiometry and the $\bar{3}$ symmetry motifs (Figure 2) which ultimately click into the Kagome pattern of dimers of Figure 1.

The remaining N−H forms a hydrogen bond with the carbonyl oxygen of another molecule (2.052 Å, ∠N−H···O, 169.1°), and, again, the $\bar{3}$ symmetry is satisfied by the creation of a centrosymmetrical hydrogen-bonded organic tubule capped by cluster anions, as depicted in Figure 3a. Thus, (111) slabs are connected solely by the latter, self-complementary N−H···O hydrogen bond motif of 3 + 3 molecules with no direct overlap between the conjugated radical cation π systems of successive slabs along the $\bar{3}$ axis. That is, there is no direct or indirect HOMO···HOMO interactions between donors of different (111) layers. Therefore, the relevant part of the electronic structure of [EDT-TTF-CONH$_2$]$_6$[Re$_6$Se$_8$(CN)$_6$] is that based on the HOMO of the donors within any two-dimensional (2D) Kagome lattice of donors only.

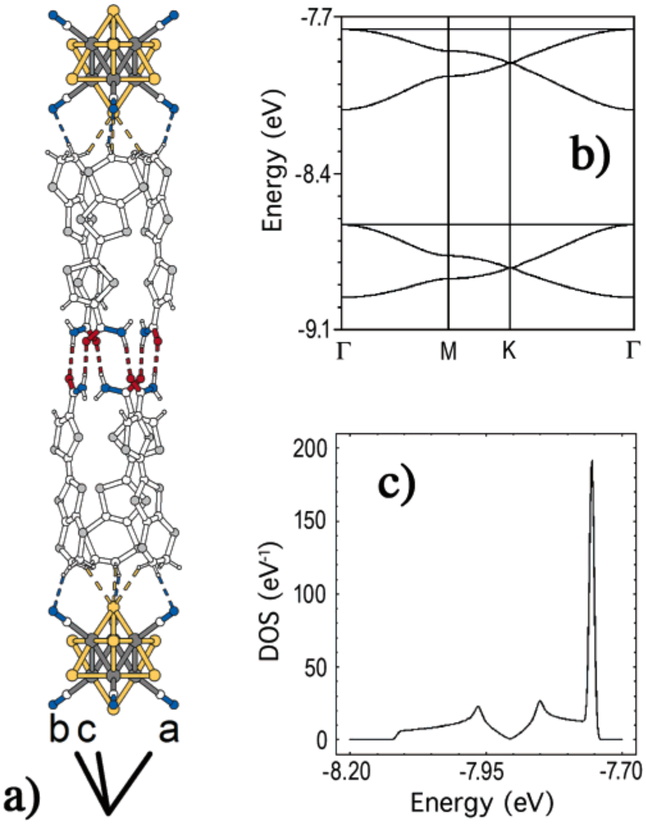

Figure 3. (a) A projection of the inter-Kagome layers motif. The connectivity along [111] is realized by association into an organic tubule of three-fold symmetry of three molecules belonging to one (111) plane with three molecules belonging to the plane below and rotated by 60°. Note the self-complementary, cyclic hydrogen-bond seam involving six N−H and six carbonyls of six molecules build out of one single N−H···O hydrogen bond (H···O, 2.052 Å; ∠N−H···O, 169.1°). Note also the two weak hydrogen bonds C−H···N (H···N, 2.383 Å; ∠C−H···N, 156.7°) and C−H···Se (H···Se, 3.069 Å; ∠C−H···Se, 146.3°) by which two cluster anions cap the opposite sets of ethylene ends of any tubule; (b) calculated band structure for the two-dimensional Kagome donor (111) slab of [EDT-TTF-CONH$_2$]$_6$[Re$_6$Se$_8$(CN)$_6$] at 293 K. $\Gamma = (0, 0)$, $M = (a'^*/2, 0)$ and $K = (a'^*/3, a'^*/3)$ where a' is the repeat vector of the Kagome lattice. (c) Electronic density of states associated with the three upper bands of b.

Because of the three-fold symmetry, only two different interactions (one intradimer and one interdimer) exist. The intradimer interaction is approximately 4 times stronger than the interdimer one (+413 vs −115 meV) because of the favorable overlap mode (in-between fully eclipsed and bond-over-ring) which leads to shorter S···S contacts. Thus, when the in-phase and out-of-phase combinations of the two HOMOs of the dimer spread into bands, the latter should remain well separated. The tight-binding band structure calculated for the 2D Kagome lattice of donors at 293 K is shown in Figure 3b. As expected, the six strongly HOMO-based bands (there are six donors per repeat unit of the lattice) appear as two distinct groups of three bands, the upper one of which is partially empty, depending on the actual charge of the octahedral cluster. The upper group of bands exhibits the typical topology of the Kagome lattice: two dispersive bands below a flat one with degeneracies at the Γ and K points.[1] The corresponding electronic density of states (DOS) is given in Figure 3c. Remarkably, the present salt, regardless of its seemingly complex structure, provides us with a textbook example of one of the simplest 2D band structures.

Balancing the Organic−Inorganic Charge Transfer between Two Electron Count Limits. A key issue now is the actual electron count ruling the collective electronic properties of this hybrid, molecular Kagome system. It is fixed by the charge balance between the two redox active components. One limit, formulated $[(\text{EDT-TTF-CONH}_2)_6{}^{3(\bullet+)}][\text{Re}_6\text{Se}_8(\text{CN}_6)^{(3-)\bullet}]$, corresponds to the case where three holes, which behave as $S = {}^1/_2$ spins, are shared by the three dimers within each unit cell, while each inorganic cluster at the center of the hexagonal motif of the Kagome lattice bears one $S = {}^1/_2$ spin. If one assumes that the electron−electron interactions are weak, the so-called weak coupling description, the upper set of bands in Figure 3b is half-filled, and one expects a metallic state. Note, however, that any half-filled band system is akin to electronic localization,[23] and the material may ultimately behave as a magnetic insulator. In the other limit, formulated $[(\text{EDT-TTF-CONH}_2)_6{}^{4(\bullet+)}][\text{Re}_6\text{Se}_8(\text{CN}_6)^{4-}]$, with fully reduced, 24-electron diamagnetic cluster cores, four holes are now shared by the three dimers in each unit cell. The Fermi level will cross exactly at the K point (Figure 3b), and the Fermi surface is reduced to a point, a situation typical of a semi-metal. Hence, one expects a strong interplay between the cluster actual redox state, the structure symmetry, and electronic properties of the material.

Because of the cluster anion $\bar{3}$ site symmetry, the different three *trans*-(Re-to-Re) distances expected[16c] for $[\text{Re}_6\text{Se}_8(\text{CN}_6)^{(3-)\bullet}]$ would be averaged, and therefore, the present data cannot provide structural evidence for the actual cluster anion charge in $[\text{EDT-TTF-CONH}_2]_6[\text{Re}_6\text{Se}_8(\text{CN})_6]$. Then, the CN vibration mode was measured on a KBr pellet by infrared spectroscopy at 2105 cm^{-1}, a value which compares well with that (2104 cm^{-1})[12] observed for $[\text{PPh}_4]_4[\text{Re}_6\text{Se}_8(\text{CN}_6)]$ and differs significantly from the signature of this mode at 2126 cm^{-1} for[16a] $[\text{PPh}_4]_3[\text{Re}_6\text{Se}_8(\text{CN}_6)]$. This indicates that a large majority of the cluster sites are occupied by the diamagnetic 24-electron cluster tetranion. Note, however, that the accuracy of the experiment does not preclude the existence of small amounts of paramagnetic clusters, $[\text{Re}_6\text{Se}_8(\text{CN}_6)^{(3-)\bullet}]$.

Single-Crystal Electron Spin Resonance. X-band electron spin resonance experiments were then carried out on single crystals of $[\text{EDT-TTF-CONH}_2]_6[\text{Re}_6\text{Se}_8(\text{CN})_6]$ aligned in the magnetic field. Note that the presence of any small amounts of $[\text{Re}_6\text{Se}_8(\text{CN}_6)^{(3-)\bullet}]$ ought to be readily detected since its resonance is expected at $g = 2.51$,[24,25] far from the $g = 2.0090$ signal observed for $\text{EDT-TTF-CONH}_2{}^{\bullet+}$ in $(\text{EDT-TTF-CONH}_2)_6\text{-AsF}_6$ or $(\text{EDT-TTF-CONH}_2)_2\text{ReO}_4$.[9]

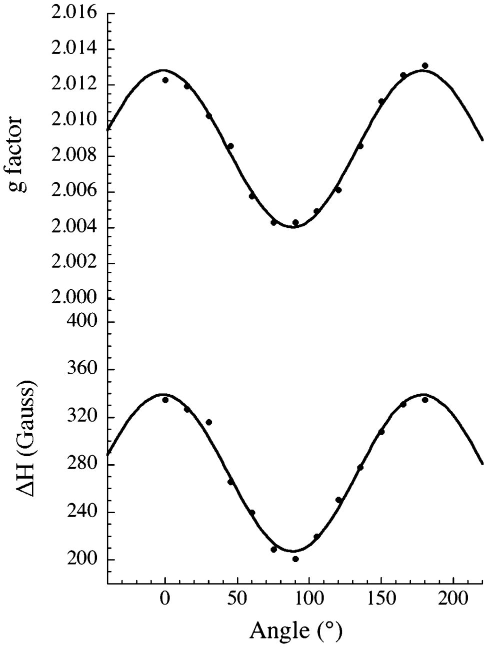

Figure 4. (Top) Room-temperature rotation pattern of the g factor with the static magnetic field applied at successive angles from the [111] direction ($\theta = 0°$) to the (111) plane ($\theta = 90°$). (Bottom) Corresponding rotation pattern for the ESR line width.

One single resonance line is observed for any orientation of the crystal. When the $\bar{3}$ axis is perpendicular to the microwave magnetic field, a Lorentzian line is observed. Figure 4 gives the corresponding measured rotation patterns for the g factor and line width (ΔH). Standard sinusoidal variations are then found with extrema along and perpendicular to the $\bar{3}$ axis. When this axis is parallel to the microwave magnetic field, both the static magnetic field and the electrical microwave field are located in the conducting (111) plane. The characteristics of the ESR line are then independent of the details of the crystal orientation, a neat illustration of the crystal symmetry. As exemplified in Figure 5, this line has a Dysonian shape at room temperature, and its asymmetry is crystal-size dependent, close to $A/B = 1.8$ for the particular sample illustrated in Figure 5.[26] Note that the fact that a Dysonian behavior is essentially observed when the microwave electric field is located in the (111) plane emphasizes the 2D character of the electrical conductivity as it reveals an intralayer conductivity much larger than along the [111] direction.

As illustrated in Figure 5 (top), this Dysonian behavior changes dramatically with temperature. The line asymmetry A/B first increases when cooling and finally decreases below 200 K. The line becomes Lorentzian within the experimental error below 150 K. As mentioned in the experimental part, the electrical conductivity can be readily deduced from the line asymmetry A/B for isotropic samples of simple shapes. We expect by symmetry an isotropic electrical conductivity in the (111) plane, and we have used the data obtained by Pifer and Magno[22] to deduce the electrical conductivity in this plane. However, the crystal shape is complicated in our case, and the determination of absolute values remains difficult. Thus, we have chosen to normalize these ESR data to the dc conductivity (see the following section). The result is shown in Figure 6a, where two different crystals were used to cover the whole temperature range (as the simple expression given in the experimental part implies moderate values of A/B). A metallic behavior is first observed upon cooling. Then, a sharp decrease

---

(23) Giamarchi, T. *Chem. Rev.* **2004**, *104*, 5037.

(24) (a) Bennett, M. V.; Beauvais, L. G.; Shores, M. P.; Long, J. R. *J. Am. Chem. Soc.* **2001**, *123*, 8022. (b) Larina, T. V.; Ikorskii, V. N.; Vasenin, N. T.; Anufrienko, V. F.; Naumov, N. G.; Ostanina E. V.; Fedorov, V. E. *Russ. J. Coord. Chem.* **2002**, *28*, 554. These authors find $g = 2.51$ at 77 K.

(25) We also have measured the ESR spectrum of a single crystal of $[\text{PPh}_4]_3[\text{Re}_6\text{Se}_8(\text{CN}_6)]$. Because of the important line width, accurate measurements are possible at low temperature only. For example, at 30 K, a nearly isotropic signal is recorded with $g = 2.50$ and a line width of 340 G. This temperature is probably optimum for this determination as the ESR line becomes asymmetric at lower temperature.

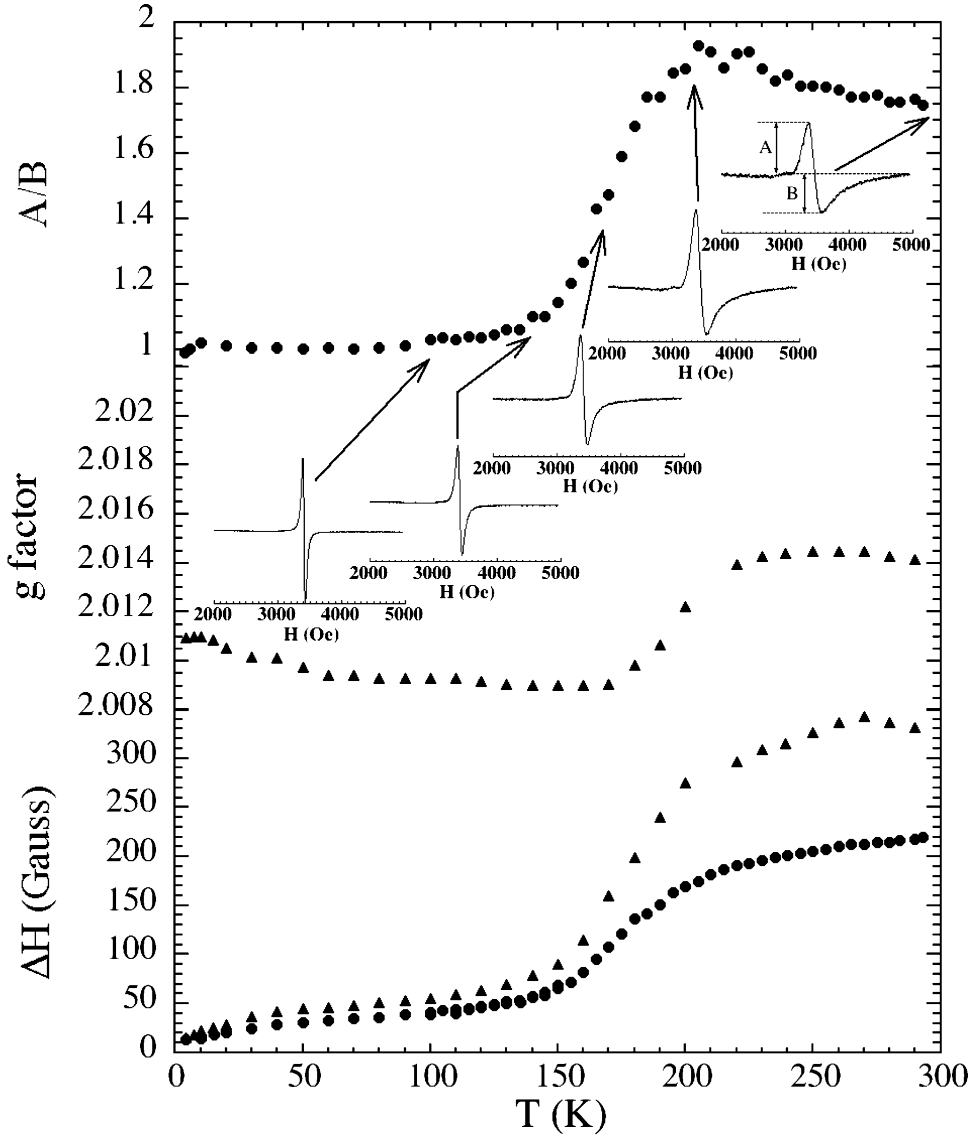

Figure 5. (Top) Temperature dependence of the asymmetry A/B of the ESR line when both the static magnetic field and the ESR electric field are applied in the (111) plane (the resonance line is shown at selected temperatures). (Middle) Temperature dependence of the *g* factor when the magnetic field is applied along the [111] direction. (Bottom) Temperature dependence of the ESR line width when the magnetic field is applied in the (111) plane (full dots) and along the [111] direction (full triangles).

of the in-plane electrical conductivity is observed below 200 K, suggesting the occurrence of a metal−insulator phase transition. Since the shape of the line is changing with temperature in this orientation, a more accurate determination of the line width and *g* factor was conducted (Figure 5) with the static magnetic field applied along the $\bar{3}$ axis, an orientation where the line remains symmetric at any temperature. A large decrease of the line width Δ*H*, associated with an important variation of the *g* factor, is observed between 200 and 150 K. A saturation of both *g* and Δ*H* is found to occur below 150 K even if some minute temperature dependence remains below 50 K. Finally, the temperature dependence of the spin susceptibility is given in Figure 7. ESR and SQUID data are consistent (the ESR data was normalized using the room-temperature SQUID value), and both indicate a clear increase of the susceptibility below 200 K which saturates below 100 K. The low-temperature part of the curve can be assigned to the presence of minute amounts of magnetic impurities. Taken together, these magnetic data are strong indication of a crossover between two different regimes between 150 and 200 K and the existence of a phase transition.

dc Electrical Conductivity. Transport measurements proved to be quite challenging because of the crystal surface sensitivity, the electronic anisotropy, and the complex shape of the crystals. They were performed down to $T \approx 80$ K by using the standard four-point dc method with a constant current of 10 or 100 μA running parallel to the most developed crystallographic plane (−100) or (010), as shown schematically in the Supporting Information. These two geometries allow measuring the electrical conductivity along two almost perpendicular directions, essentially parallel and perpendicular to the isotropic plane (111), respectively. Electrical contacts between the platinum wires (20 μm in diameter) and the crystal surface have been prepared with a graphite paste. Note that the as-grown crystal surface became poorly conducting in time with the contact resistance reaching a few tens to hundreds of kiloohms, while after the surfaces were polished, the contacts resistance decreased down to 20−

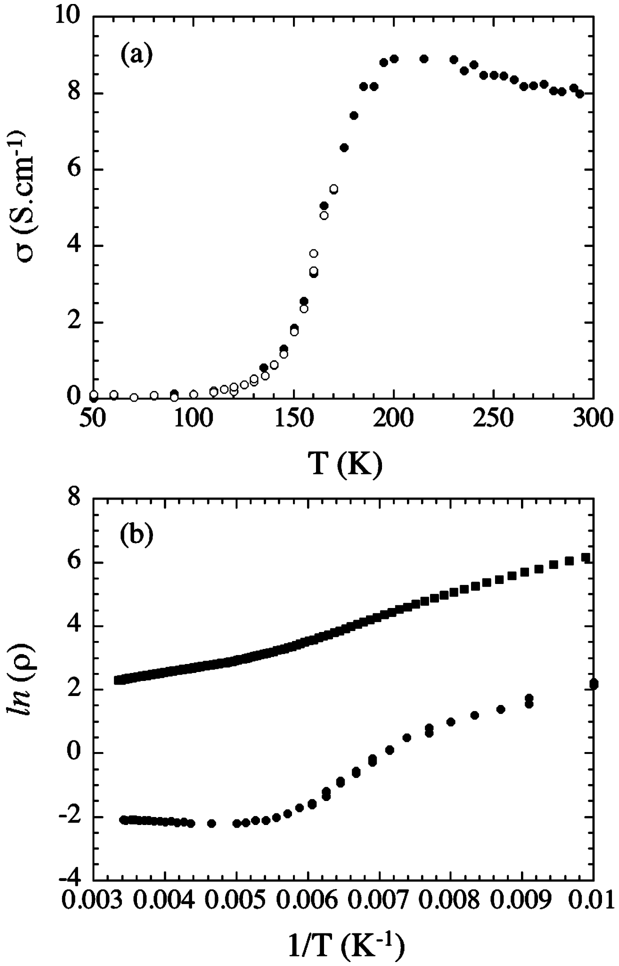

Figure 6. (a) Electrical conductivity deduced from the ESR line asymmetry. The absolute value was obtained by normalization with the low-temperature dc data. Open and full symbols correspond to two different crystals; (b) semilog plot of the resistivity parallel (full dots, ESR data) and perpendicular (full squares, dc data) to the conducting (111) planes. Note the activated behavior at low temperature, with similar values of the activation energy.

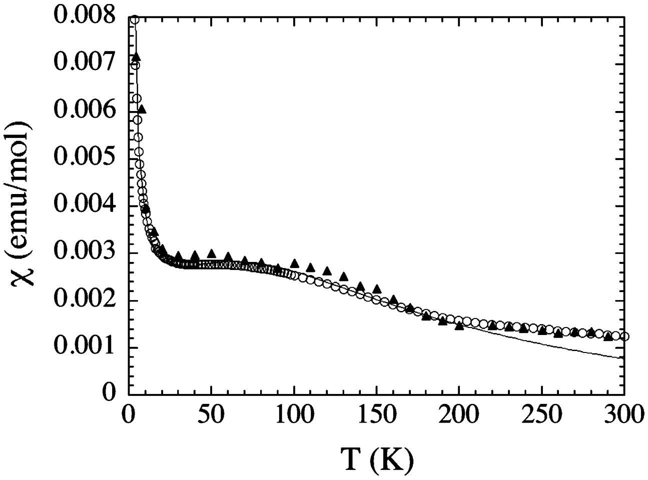

Figure 7. Temperature dependence of the spin susceptibility (open dots: SQUID measurement; full triangles: ESR data). The ESR data have been normalized to the 300 K SQUID value. The continuous line is the fit to a uniform chain of $^1/_2$ spins augmented of a Curie component, as discussed in the text.

30 Ω. Therefore, the most developed crystal faces, (−100) or (010), were systematically polished prior to installing the set of contacts. The room-temperature conductivity was found to be ca. $\sigma_{(111)} \approx 3\ \Omega^{-1}\ \mathrm{cm}^{-1}$ in a direction almost parallel to the isotropic crystallographic plane (111) and ca. $\sigma_{[011]} \approx 0.1\ \Omega^{-1}\ \mathrm{cm}^{-1}$ in an almost perpendicular direction. Despite our efforts to optimize the measurements, we never obtained the high-temperature metallic behavior revealed by ESR in the (111) plane. Instead, we found a semiconducting variation of the conductivity whose activation energy is small, of the order of 27 meV. However, the dc and ESR data become consistent below 130 K where a semiconducting behavior is found with a common activation energy of about 70 meV. Thus, the surface sensitivity and the likely presence of small amounts of defects as a result of polishing are presumed to preclude the measurement of the intrinsic in-plane conductivity at high temperature. Therefore, only the ESR data is shown in Figure 6b for that orientation. Note that we have used the low-temperature dc data to normalize the ESR curve in Figure 6. This gives a room-temperature conductivity value of $8\ \Omega^{-1}\ \mathrm{cm}^{-1}$, i.e., 2.6 times larger than the dc estimation. The typical temperature dependence of the perpendicular resistivity is also given in Figure 6b. In this case, the absolute value is larger, and we expect this result to be intrinsic. This semilog plot also gives an S-shape, confirming the analysis deduced from ESR data. Note that the activation energy is the same in both orientations in the low-temperature phase.

Taken together, ESR and dc data strongly suggest the occurrence of a metal−insulator phase transition between 150 and 200 K. Low-temperature X-ray and ^{1}H spin−lattice relaxation experiments were then performed to probe this assumption and will now be discussed successively.

A Triclinic Structure at 100 K. Consistent with its metal−insulator phase transition, single-crystal X-ray data collected on (EDT-TTF-CONH$_2$)$_6$[Re$_6$Se$_8$(CN)$_6$] revealed a triclinic $P\bar{1}$ structure at 100 K (Figures 8 and 9) whose asymmetric unit contains one cluster anion and three independent EDT-TTF-CONH$_2$ molecules, all in general position. As exemplified in Figure 8a, the conformation and orientation of one out of the three independent dimers is now found to differ from the other two.

X-ray diffuse scattering experiments gave evidence, collected in the Supporting Information, for the presence of split Bragg reflections at low temperature consistent with the appearance of domains and the observed large increase in crystal mosaicity. Investigations of the structural phase transition by temperature-dependent X-ray powder diffraction experiments are currently under way in our laboratories. As shown in Figure 9, one dimer is fully oxidized and formulated [EDT-TTF-CONH$_2$]$^{2+}$, the other two mixed-valence dimers, [EDT-TTF-CONH$_2$]$^{\bullet+}$, remaining essentially unaffected across the phase transition.

Because of the loss of the three-fold axis the purely π-donor sublattice is now associated with three different intradimer and interdimer interactions. The intradimer transfer integrals of dimers A, B, and C are calculated to be +413, +587, and +414 meV, respectively. The three interdimer transfer integrals are −131, −112, and −119 meV. Let us remind that the intradimer and interdimer transfer integrals for the high-temperature phase are +413 and −115, respectively. Thus, whereas the interdimer interactions do not change very strongly, one of the three intradimer interactions, that associated with dimer B, becomes noticeably stronger. Although the relatively low quality of the

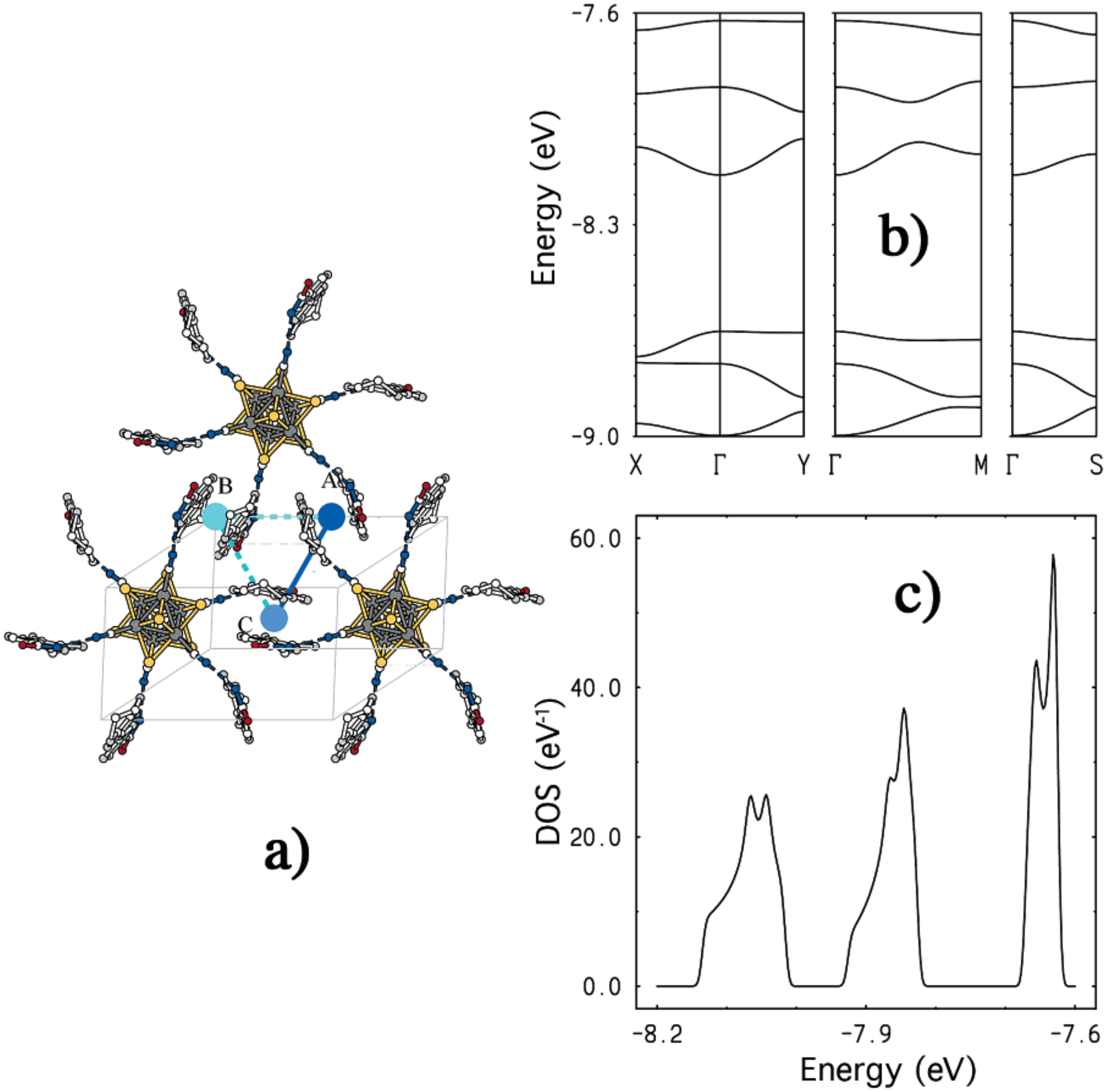

Figure 8. (a) Projection of the 100 K crystal structure down onto the layer shown in Figure 9. Note that the three types of dimers A (symbolized by a blue ball in its center), B (cyan ball), and C (darker cyan ball) are all different in this triclinic distortion of the former rhombohedral system. Note also the offset and singular conformation of the fully oxidized dimer B. (b) Calculated band structure for the distorted 2D Kagome donor (111) slab of [EDT-TTF-CONH$_2$]$_6$[Re$_6$Se$_8$(CN)$_6$] at 100 K. $\Gamma = (0, 0)$, $X = (a'^*/2, 0)$, $Y = (0, b'^*/2)$, $M = (a'^*/2, b'^*/2)$ and $S = (-a'^*/2, b'^*/2)$ where a' and b' are the repeat vectors of the distorted Kagome lattice. (c) Electronic density of states associated with the three upper bands of (b).

structure would make an in-depth analysis of the origin of these variations not reasonable, it is clear that the increase in the intradimer interaction B is associated with the fact that the two molecules have moved to the point where this dimer is now half-eclipsed (see Figure 9), leading to very favorable S···S orbital interactions.

The calculated band structure for the distorted Kagome lattice at 100 K is shown in Figure 8b. As for the high-temperature structure, the six bands are separated in two groups of three bands because the intradimer interactions are considerably stronger. However the three bands of a group are separated by energy gaps because of the loss of the three-fold axis. The DOS associated with the three upper bands is reported in Figure 8c. Analysis of the nature of the wave vectors for different points of the Brillouin zone clearly shows that the upper band originates almost completely from the antibonding combination of the HOMOs of the two donors in dimer B. In contrast, the remaining two bands originate from the antibonding combination of the HOMOs of the donors in dimers A and C. Thus, it is clear that dimer B is associated with a 2+ charge, whereas dimers A and C are associated with a 1+ charge. We are now ready for a discussion of the relationship between the evolution of the structure and ground state of (EDT-TTF-CONH$_2$)$_6$[Re$_6$Se$_8$(CN)$_6$] which we now address from the point of view of the resonance of the ^{1}H sites in the solid state.

^{1}H spin−lattice relaxation in [EDT-TTF-CONH$_2$]$_6$[Re$_6$Se$_8$(CN)$_6$]. The ^{1}H sites have been shown to be good probes of the molecular motion in molecular conductors,[27] and generally speaking, solid-state NMR proved to be very efficient in unraveling the intricate physical properties of the low dimensional organic conductors.[28,29] We have therefore studied the resonance of protons located on the ethylene groups in [EDT-

---

(26) To avoid a large distortion of the line shape, this study was made with a small single crystal. We have checked that the resonance line has a larger asymmetry for bigger crystals.

(27) Wzietek, P.; Mayaffre, H.; Jérome, D.; Brazovskii, S. *J. Phys. I France* **1996**, *6*, 2011.

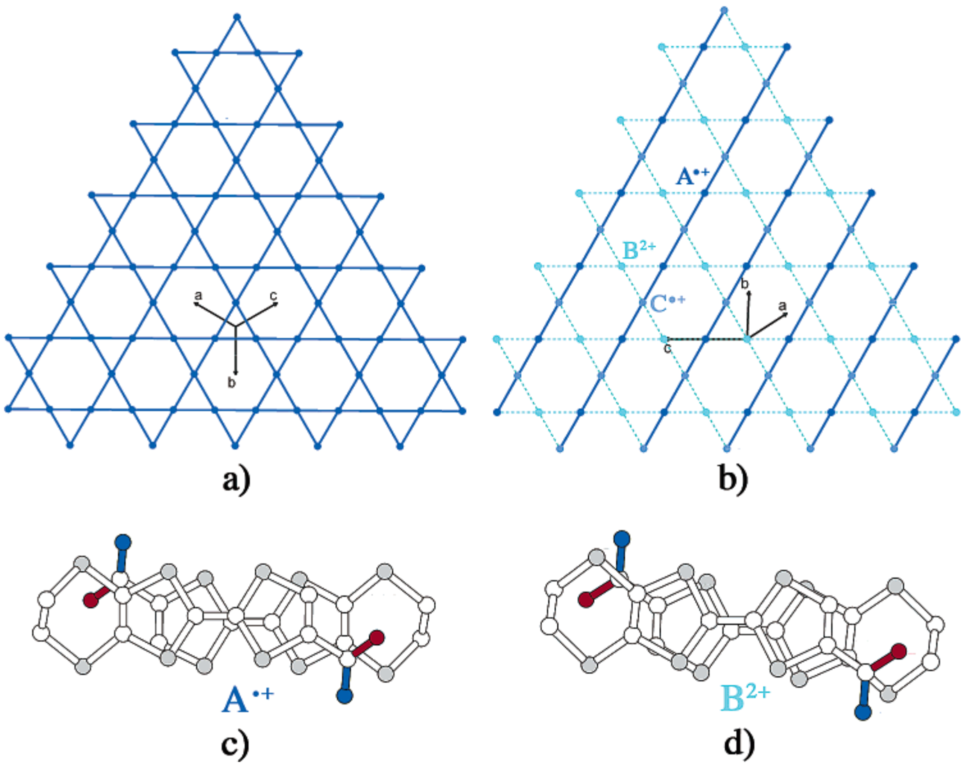

Figure 9. The symmetry of the Kagome net in the rhombohedral room-temperature structure (a) is broken in the triclinic structure at 100 K (b). The distortion essentially results from a molecular motion and a net change of conformation, shown in Figure 8, of dimer B (cyan sites), in response to the localization of one extra hole on any of these sites—a seemingly slight local adjustment associated with singular long-range cooperative structural and electronic effects. Note that the slipped pattern of intra-dimer overlap of dimers A (c) and C is essentially unaffected by the transition while dimer B (d) is now half-eclipsed which makes for a stronger intradimer HOMO···HOMO interaction. The transition leaves only one single direction of 1D uniform chains of spins $^1/_2$, materialized by the parallel solid blue lines (b); charge ordering has occurred along the two broken cyan line directions—materialized by two slightly different tones of cyan in (b)—where $A^{\bullet+}$ (or $C^{\bullet+}$) and B^{2+} alternate.

TTF-CONH$_2$]$_6$[Re$_6$Se$_8$(CN)$_6$]. NMR experiments have been conducted on one single crystal in a standard NMR pulsed spectrometer at different magnetic fields (9.3, 2, and 1 T) in the temperature domain 320−5 K. The ^{1}H relaxation data displayed in Figure 10 show quite interesting temperature- and field-dependent events. First, a field-dependent relaxation peak is observed between 200 and 300 K; then, the relaxation is found to become independent of temperature but is still field dependent between 2 and 9 T, and finally, a low-temperature peak takes place whose position is also strongly field dependent.

The high-temperature relaxation peak is very reminiscent of the peak observed in the ^{1}H relaxation study performed on κ-(ET)$_2$Cu[N(CN)$_2$]Br, a 2D organic compound containing ethylene groups.[27] Hence, similar interpretations are very likely. At high temperature, the position of the (CH$_2$)$_2$ groups at the end of the EDT molecules fluctuates with a thermally activated correlation time. Consequently, the relaxation time of the protons of the (CH$_2$)$_2$ groups is induced by the dipolar coupling between protons when the nuclear Larmor frequency is comparable with the frequency of these fluctuating dipolar couplings. Following the standard BPP theory[30] the resulting relaxation rate reads,

$$1/T_1 \propto \frac{a}{1+\omega_n^{\,2}\tau_c^{\,2}} \text{ with } \tau = \tau_0 \exp\frac{E_a}{kT}$$

where E_a is the activation energy for the motion of the (CH$_2$)$_2$ groups and a characterizes the amplitude of the dipolar coupling between ^{1}H nuclei. Figure 10 also shows the fit of the $1/T_1$ data to the BPP theory with the set of parameters $a = 4.3 \times 10^9$ s^{-2}, $\tau_0 = 7 \times 10^{-14}$ s, and $E_a = 2700$ K. Note that a similar activation energy has been reported for κ-(ET)$_2$Cu[N(CN)$_2$]Br.[27] The motion-induced relaxation, although dominant above 200 K (especially at low fields), becomes negligible at lower temperatures when the relaxation is temperature independent. The low-temperature contribution can then be ascribed to a relaxation of hyperfine origin between electrons and nuclear spins. Furthermore, it is seen that the low-temperature relaxation rate is field dependent at high fields (above 2 T).

The intermediate temperature regime ($50 < T < 175$ K) can be compared to the behavior of the ^{1}H relaxation in one-dimensional (1D) organic compounds such as (TMTTF)$_2$Br or (TMTTF)$_2$PF$_6$ under pressure.[28] However, in the latter, the protons belong to CH$_3$ groups which are known to provide several relaxation peaks in temperature due to the classical and the quantum rotations of CH$_3$ groups. But outside the temperature domains in which the relaxation is dominated by motion, $1/T_1$ is temperature independent as observed for (TMTTF)$_2$Br at 1 bar or (TMTTF)$_2$PF$_6$ under 13 kbar.

The behavior of the relaxation reinforces the physical picture derived from the crystal structures and electronic band structure calculations and the transport, ESR, and susceptibility studies. A temperature independent contribution to $1/T_1$ is expected for the case of strong 1D antiferromagnetic (AF) fluctuations, as suggested by the early calculations of Hone and Pincus.[31] For

---

(28) Wzietek, P.; Creuzet, F.; Bourbonnais, C.; Jérome, D.; Bechgaard, K.; Batail, P. *J. Phys. I France* **1993**, *3*, 171.
(29) Miyagawa, K.; Kanoda, K.; Kawamoto, A. *Chem. Rev.* **2004**, *104*, 5635.
(30) Abragam, A. *The Principles of Nuclear Magnetism*; Clarendon Press: Oxford, 1961.

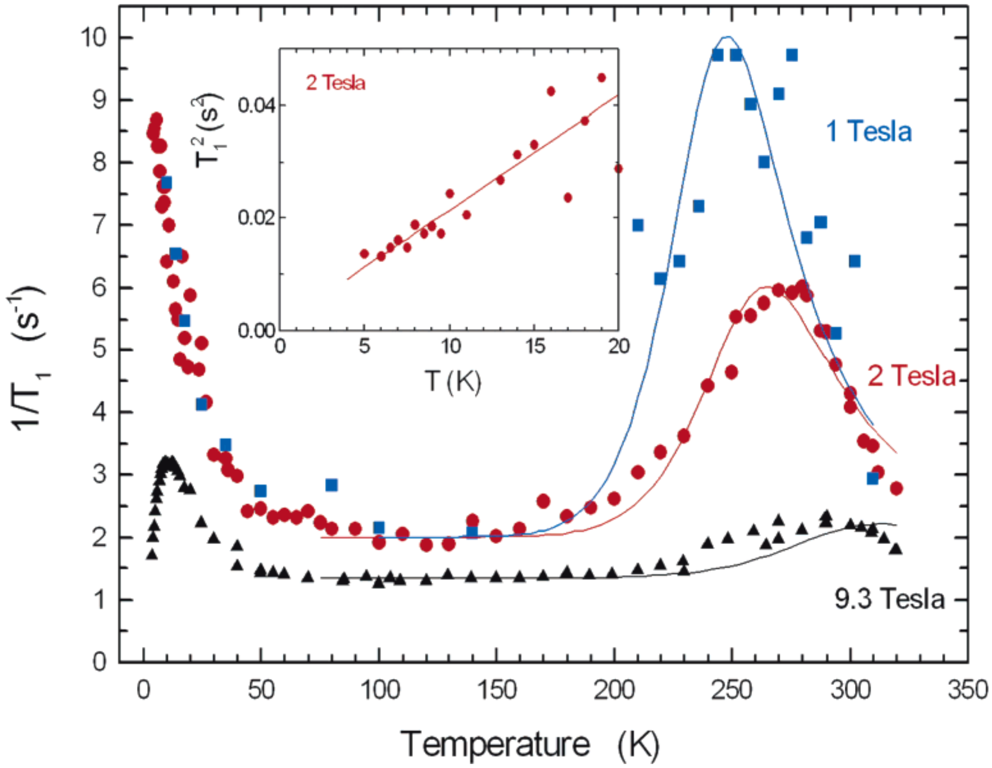

Figure 10. Temperature dependence of the proton spin−lattice relaxation rate, $1/T_1$, measured at different magnetic fields: (■) 1 T, (●) 2 T, and (▲) 9.3 T. (Inset) Linear fit of T_1^2 versus T in the low-temperature region for the $H = 2$ T data.

the case of Heisenberg chains of spins $S = {}^1/_2$ or in the strong coupling limit of the half-filled band Hubbard model, $1/T_1$ reads A^2/J in the low-temperature limit (with $J \approx t^2/U$ in the Hubbard model). This value is indeed strongly enhanced with respect to the case of a delocalized electron gas where $1/T_1 \propto T/E_F\ A^2/E_F$. Furthermore, the frequency dependence of T_1 below 200 K provides additional information. The frequency dependence is the signature of a low dimensional spin motion. This has been widely studied in the case of 1D conductors[32] and also in 1D Heisenberg chains.[33,34] A frequency dependence in the form, $1/T_1 \propto H^{-1/2}$, is expected from the long time dependence of the spin−spin correlation functions which decays such as $t^{-1/2}$ as $t \rightarrow \infty$ in one dimension leading to a diverging $1/T_1$ as $H \rightarrow 0$. In real systems the divergence of $1/T_1$ as $H \rightarrow 0$ is cutoff by the existence of an interchain spin coupling, $J_\perp$, removing the 1D character of the spin motion. Thus, the present NMR experiments have provided the important confirmation for the existence of weakly coupled Heisenberg chains below 200 K.

At low temperature a steep rise of $1/T_1$ is observed without any peak down to 5 K at 1 and 2 T but with a sharp peak around 12 K at 9.3 T. As molecular motions can be ruled out at such low temperatures, the upturn of the relaxation can be ascribed to a slowing down of AF fluctuations. These magnetic fluctuations induce in turn a nuclear spin relaxation via the modulation of the hyperfine electron-nucleus coupling. Although the AF fluctuations have a broad spectrum, the physics of the phenomenon can be qualitatively captured by a BPP-like approach, i.e., assuming a single correlation time. Hence, at low fields, the relaxation rate remains in the regime $\omega_e\tau \ll 1$ down to 5 K while this is no longer true at 9.3 T where $1/T_1$ reaches its maximum between 10 and 12 K, which signals the situation $\omega_e\tau = 1$. Having said that, we should make another comment here. Frequency (field) dependent relaxation is generally expected when the characteristic frequencies of the system approach the Larmor frequency. This is often seen in relaxation caused by fluctuations in the vicinity of a conformational ordering, because the characteristic time of fluctuations between two metastable configurations diverges at the freezing point. As for spin fluctuations, however, such an analogy is too naive because then we are rather in the limit where all frequencies of the system are much higher than ω_e. In this case, NMR relaxation operates essentially in a region of “white noise” corresponding to the zero frequency limit of the spectrum, and T_1 is independent of the frequency. This is usually the case for magnetic transitions because the electronic frequencies are so high that they never reach the regime $\omega_e\tau = 1$, even within a critical region. For example, we do not observe any field dependence in the $1/T_1$ peak at a spin density wave (SDW) transition in 1D organics.[35] On the other hand, such a dependence is often seen in “glassy” transitions because these exhibit a broad range of fluctuation time scales extending to very low frequencies. Accordingly, when a SDW transforms to a spin glass, a huge field dependence[36] is observed. The situation is somewhat similar in frustrated spin systems.[37] Therefore, we

---

(31) Hone, D. W.; Pincus, P. *Phys. Rev. B* **1973**, *7*, 4889.
(32) Soda, G.; Jérome, D.; Weger, M.; Alizon, J.; Gallice, J.; Robert, H.; Fabre, J.-M.; Giral, L. *J. Phys.* **1977**, *38*, 931.
(33) Boucher, J. P.; Ferrieu, F.; Nechtschein, M. *Phys. Rev. B* **1974**, *9*, 3871.
(34) Borsa, F.; Mali, M. *Phys. Rev. B* **1974**, *9*, 2215.
(35) Clark, W. G.; Hanson, M. E.; Alavi, B.; Moulton, W. G.; Kuhns, P.; Reyes, A. *Synth. Met.* **1999**, *103*, 2166−2167.
(36) a) Nomura, K.; Kubota, H.; Kotomizu, M.; Hanajiri, T.; Nakatsuji, S.; Yamada, J. *Synth. Met.* **2003**, *19*−*21*, 133−134. (b) Matsunaga, N.; Hosokawa, Y.; Iwasaki, H.; Nomura, K.; Takasaki, S.; Yamada, J.; Nakatsuji, S.; Anzai, H.; Nakamura, T.; Takahashi, T.; Saito, G. *J. Phys. IV* **1999**, *9*, Pr10−243.

might believe that this compound presents some signs of magnetic frustration.

If we attempt a power law analysis of the relaxation, a square root divergence of $1/T_1$ can be fitted at low temperature (see insert of Figure 10). However, if any finite ordering temperature exists it should be very low (of the order of 1 K or less). Such a low ordering temperature would compare fairly well with the long-range ordering observed at 0.49 K in Tanol[33] given in chain and interchain coupling constants of 65 and 10^{-2} K, respectively, for $[\text{EDT-TTF-CONH}_2]_6[\text{Re}_6\text{Se}_8(\text{CN})_6]$.

Note finally that proton relaxation does not allow for a direct investigation of the electron localization on account of the large contribution due to the ethylene motion occurring precisely in the same temperature domain. However, it is of interest to note that the experimental relaxation rate above 300 K (Figure 10) is always lower than the prediction from a BPP contribution plus the constant hyperfine term of low temperature. This is an indication for a decrease of the hyperfine contribution moving to high temperatures which is in line with the decrease of the electron spin correlation time, $\tau_c = h/J$ (h/E_F) below (above) 200 K.

Analysis of the ESR of the High-Temperature, Rhombohedral Phase. The fact that one single resonance is recorded above 180 K is an indication that the signal is an admixture of organic and inorganic spins resonances. The observation of an hybrid resonance qualifies the existence of some amounts of $[\text{Re}_6\text{Se}_8(\text{CN}_6)^{(3-)\bullet}]$ at room temperature. Since only one single line is present, the contributions of the organic and inorganic spins to the resonance are coherently mixed. A quantitative analysis of this admixture can be made in the case a Lorentzian line, that is, in our case, when the magnetic field is applied along the $\bar{3}$ axis.[38,39] The most accurate analysis concerns the g factor which is expected to be temperature independent for both the organic and the inorganic species. The net g factor reads:

$$g(T) = x(T)g_{\text{org}} + (1 - x(T))g_{\text{inorg}} \tag{1}$$

where

$$x(T) = \chi_{\text{org}}(T)/(\chi_{\text{org}}(T) + \chi_{\text{inorg}}(T))$$

Reasonable values are $g_{\text{org}} = 2.0090$,[21] and $g_{\text{inorg}} = 2.5$.[24,25] The organic and inorganic contributions to the spin susceptibility are separated by exacting the sum $\chi_{\text{org}}(T) + \chi_{\text{inorg}}(T)$ to the experimental spin susceptibility. As the inorganic cluster spins should behave like localized spins, we expect their magnetic susceptibility to follow a Curie law, i.e., $\chi_{\text{inorg}}(T) = 0.375/T$ emu mol^{-1}. With these assumptions, the density of inorganic paramagnetic objects reads $n(T) = T\chi_{\text{inorg}}(T)/0.375$ (Figure 11) and amounts to ca. 1% of $[\text{Re}_6\text{Se}_8(\text{CN}_6)^{(3-)\bullet}]$ at room temperature. Moreover, this number decreases rapidly upon cooling, and the paramagnetic clusters become undetectable within the experimental error in the low-temperature phase. The temperature dependence observed for $n(T)$ suggests a critical effect due to the presence of the structural phase transition. For example, the solid line in Figure 11 is a fit based on:

$$n(T) = a\sqrt{T - T_C} \tag{2}$$

with $a = 0.001$ and $T_C = 180$ K.

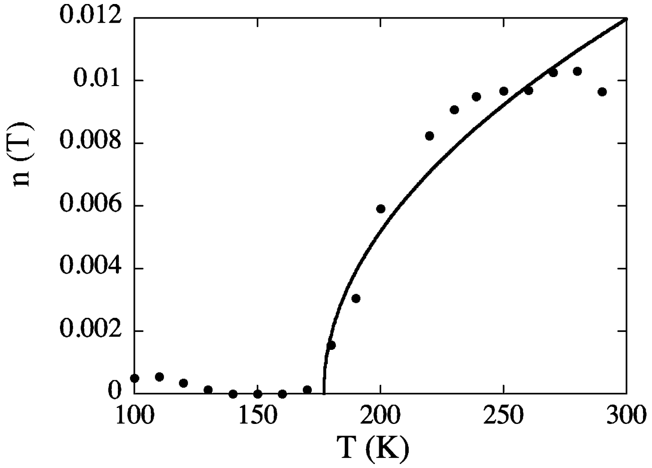

Figure 11. Evolution of the number $n(T)$ of $[\text{Re}_6\text{Se}_8(\text{CN})_6^{(3-)\bullet}]$ clusters per mole as the temperature is lowered, as determined from ESR data. The continuous line is the fit to a square root temperature dependence, as discussed in the text.

A similar, albeit less accurate determination of $n(T)$ is possible from a line width analysis providing the temperature dependence of ΔH for each magnetic ion is known.[38,39] In our case, the cluster line width is too large to be measured above 100 K. A crude analysis can be made doing a linear extrapolation of the low-temperature data, yielding a value of $n(T)$ also of the order of a few percent at 300 K and decreasing quickly when cooling. This is already evident in Figure 5 as the temperature dependence of ΔH mimics that observed for $g(T)$.

The square root dependence of the density $n(T)$ of inorganic paramagnetic objects can be explained using simple arguments. Independently of the details of the phase transition mechanism, its diminution reflects an inherent instability of the system whose symmetry is broken and implies the existence of an order parameter, called M in the following. In this context, the number of $[\text{Re}_6\text{Se}_8(\text{CN}_6)^{(3-)\bullet}]$, n, plays the role of a secondary order parameter coupled to M through a coupling term of the form:

$$\Delta F = \lambda M^2 n \tag{3}$$

where λ is a coupling constant (positive as the equilibrium value of n vanishes in the low-temperature phase).

Above T_C, the average value of M is zero, but the average of M^2, $\langle M^2 \rangle$, remains relevant. The simplest (mean field) approximation consists of the substitution of ΔF for:[40]

$$\Delta F_{\text{MF}} = \lambda \langle M^2 \rangle n \tag{4}$$

In the above expression, $\lambda\langle M^2 \rangle$ plays the role of an effective, temperature-dependent energy for any $[\text{Re}_6\text{Se}_8(\text{CN}_6)^{(3-)\bullet}]$. Moreover, the mean field approximation gives:[41]

$$\langle M^2 \rangle = K\left[1 - \left(\frac{T - T_c}{T}\right)^{1/2}\right] \tag{5}$$

where K is the value of $\langle M^2 \rangle$ at T_C.

---

(37) See, for example, Hamad, I. J.; Trumper, A. E.; Wzietek, P.; Lefebvre, S.; Manuel, L. O. *cond-mat*/0501146.

(38) Carrington A.; McLachlan, A. D. *Introduction to Magnetic Resonance*; Harper and Row: New York, 1966.

(39) Such an analysis was made, for example, for TTF-TCNQ: Tomkiewicz, Y.; Taranko, A. R.; Torrance, J. B. *Phys. Rev. Lett.* **1976**, *36*, 751.

(40) See, for example, Chaikin, P. M.; Lubensky, T. C. *Principles of Condensed Matter Physics*; Cambridge University Press: New York, 1998.

(41) Prost, J.; Barois, P. *J. Chim. Phys.* **1983**, *80*, 65.

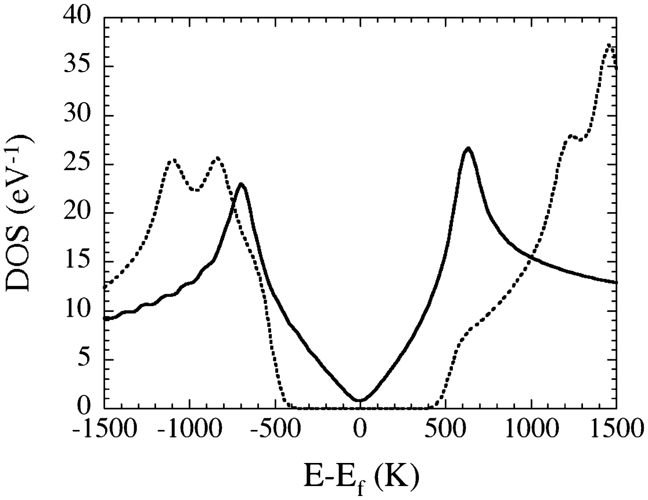

Figure 12. Zoom of the electronic density of states close to the Fermi energy for the high-temperature phase (continuous line) and low-temperature phase (dotted line). In both cases, the Fermi energy corresponds to a band filling of four holes (two electrons) per unit cell.

Finally, the effective energy of any $[Re_6Se_8(CN_6)^{(3-)\bullet}]$ varies like:

$$\epsilon(T) = \epsilon_c - K\lambda\left(\frac{T - T_c}{T}\right)^{1/2} \qquad (6)$$

The latter is introduced in the Boltzmann law to yield $n(T)$ as a first order in λ and for temperatures close to T_C:

$$n(T) = n_c + a(T - T_c)^{1/2} \qquad (7)$$

This expression is consistent with the experimental data if n_C is very small.

Below the Structural Phase Transition. As the number of $[Re_6Se_8(CN_6)^{(3-)\bullet}]$ is negligible in the low-temperature phase, the Fermi level has been positioned accordingly, that is assuming four holes on each set of three dimers, $[EDT\text{-}TTF\text{-}CONH_2]_6$ (Figure 12). The important point is the existence of a gap of about 900 K at the Fermi level. It is tempting to associate this gap with the observed temperature dependence of the electrical conductivity. However, the spin susceptibility is not activated below T_C, and the band approximation fails to explain the whole set of data. As usual for organic conductors, this decoupling between charge and spin degrees of freedom is the result of sizable electron−electron interactions.[23,42] The latter affect the value of the room-temperature spin susceptibility. Using the high-temperature density of states, we have calculated its value when electron interactions are ignored.[43] For the expected amounts of $[Re_6Se_8(CN_6)^{(3-)\bullet}]$, the value of the spin susceptibility is ca. 4 times smaller than the experimental one (compare Figure 13 to Figure 7). This Pauli value remains too small even when exploring unphysical band fillings, that is, for different, meaningless electron counts. The observed large spin susceptibility is the manifestation of significant electron interactions.[44] In fact, the low-temperature spin susceptibility data can be fairly well described in the strongly localized limit. The continuous line in Figure 7 gives the best fit to a Heisenberg spin chain with $J/k_B = -65$ K, introducing 6% of non interacting spins $^1/_2$ to account for the low-temperature Curie tail.[45]

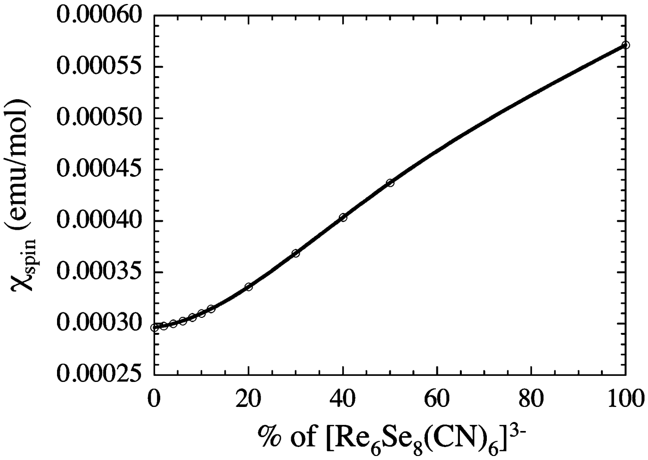

Figure 13. Calculated spin (Pauli) susceptibility at 300 K as a function of the relative amounts of $[Re_6Se_8(CN_6)^{(3-)\bullet}]$ clusters.

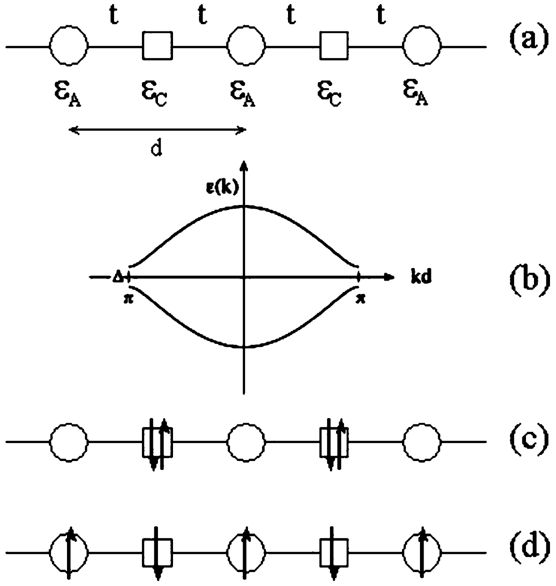

Figure 14. (a) Simple 1D model describing the electronic properties below the structural phase transition; (b) corresponding 1D band structure; (c) ground state for $t = 0$ and $U = 0$; (d) ground state for $t = 0$ and $U > \Delta$ (energy difference between the site energies of dimers A and C).

This analysis is entirely consistent with the presence in the structure at 100 K of uniform parallel rows where two kinds of nonequivalent mixed valence dimers, $[(EDT\text{-}TTF\text{-}CONH_2)_2{}^{\bullet+}]$, labeled A and C, alternate (Figure 8). These discrete chains, materialized by the solid red lines in Figure 9, are well apart in the lattice as they are interspersed between fully oxidized, diamagnetic dimers, $[(EDT\text{-}TTF\text{-}CONH_2)_2{}^{2+}]$, labeled B in Figure 9, and inorganic cluster anions. Note that along any 1D chain, dimers A and C are different but connected by a unique transfer integral t, hence the simplified model drawn in Figure 14a. Distinct sites energies (ϵ_A and ϵ_C) have been introduced to discriminate between A and C.

The corresponding 1D band structure is given in Figure 14b, where $\epsilon_A = \Delta/2$ and $\epsilon_C = -\Delta/2$. We effectively obtain a gap

---

(42) Baudron, S. A.; Avarvari, N.; Batail, P.; Coulon, C.; Clérac, R.; Canadell, E.; Auban-Senzier, P. *J. Am. Chem. Soc.* **2003**, *125*, 11583.

(43) Details of calculations are available in ref 42.

(44) Torrance, J. B.; Tomkiewicz, Y.; Silverman, B. D. *Phys. Rev.* **1977**, *B15*, 4738.

(45) The coupling between a pair of parallel adjacent spins is $-2J$; the fit was made imposing $g = 2$ and introducing a diamagnetic component $\chi_{dia} = -1.1 \times 10^{-3}$ emu/mol.

at the Fermi level, of amplitude Δ, as only the lower band is filled; thus, this simplified band model also predicts a diamagnetic ground state.

Further Discussion of Electron Interactions in the One-Dimensional Low-Temperature Phase. In the $t = 0$ limit, the ground state (for $\epsilon_A > \epsilon_C$) is depicted in Figure 14c. The two holes are localized on the most favorable site (C with our energy choice); the ground-state energy per pair A−C amounts to $-\Delta$, and this state is diamagnetic. The first excited state of a pair A−C is obtained by allowing one hole on each dimer (see Figure 14d), and its energy is 0. Thus, transfer of one hole from C to A costs the energy Δ. To discuss the effect of electron interactions, one has to consider a finite value of U, the on-site Coulombic repulsion. Thus, the energy per pair A−C for the previous ground state (Figure 14c), which implies double occupancy, becomes $U - \Delta$, while the energy of the state shown in Figure 14d remains the same. The energy difference between these two states becomes $\Delta - U$, and the state shown in Figure 14d becomes the ground state as soon as U becomes larger than Δ. As the band structure calculation gives a small gap, $\Delta \approx 0.07$ eV, we expect to be in this case, considering the values of U usually found in organic solids (typically 0.4 eV).[44] It is therefore reasonable to find experimentally that the low-temperature phase is paramagnetic. However, the electronic configuration displayed in Figure 14d represents the situation of a half-filled band (with one carrier per site (dimer)). The T_1 data below 200 K have shown that the paramagnetic state corresponds to a 1D Heisenberg chain in which the carriers are localized by the existence of strong correlations. They are also in agreement with the fit of the spin susceptibility data, shown in Figure 7, which models the magnetism of the low-temperature phase in terms of a uniform chain of spins. Hence, the gap of ca. 1000 K derived from EPR and transport data can be ascribed to a Mott localization. [EDT-TTF-CONH$_2$]$_6$[Re$_6$Se$_8$(CN)$_6$] is a material in which the value of U is of the order of the electron bandwidth calculated in Figure 3b. In addition, the introduction of a finite value of t signals the existence of antiferromagnetic interactions between the dimers (of the order of t^2/U), but the strong 1D character of the magnetic lattice suppresses the existence of any magnetic phase transition down to low temperature.

Comments on the Nature of the Phase Transition. The transition from a 2D conducting electronic regime to a 1D insulating electronic ground state occurs in synchronicity with a structural transition which goes along with the sliding motion of the molecules within one dimer only. In the process, full charge delocalization among the sets of three equivalent, mixed-valence slipped dimers of the conjugated Kagome net (Figures 1and 9a), transforms into a pattern of charge ordering along the two broken cyan lines of Figure 9 which connect one fully oxidized, now essentially eclipsed (Figure 9c) dimers B^{2+} with any of the two, essentially unaffected, slipped mixed valence dimers A$^{\bullet+}$ and C$^{\bullet+}$ (Figure 9b). In a sense, the transition breaks the conjugated, extended π system and distorts the lattice (Figure 9). Hence, the four holes present in the unit cell at low temperature are inhomogeneously distributed among the three dimers. In fact, this charge disproportionation takes the form of stripes as the segregation of the charges occurs along lines, materialized by the solid and broken lines along three different orientations in Figure 9, and is reminiscent of the one observed in several series of 2D organic conductors at the Mott transition.[46−48] We therefore suggest that the phase transition accompanying the sliding motion within one out of the three dimers in [EDT-TTF-CONH$_2$]$_6$[Re$_6$Se$_8$(CN)$_6$] is also a Mott localization. Here, the mechanism of the phase transition relies on a competition between electron−electron interactions (which promotes the localization, i.e., the low-temperature phase) and entropy which favors the high-symmetry phase. It illustrates the benefit of having engaged such unique, mineral and molecular redox cluster anions as the net entropy gained by mixing a few [Re$_6$Se$_8$(CN$_6$)$^{(3-)\bullet}$] between many more of the same, isosteric and isostructural [Re$_6$Se$_8$(CN$_6$)$^{4-}$], certainly plays an important role, as illustrated in Figure 11 where the number of [Re$_6$Se$_8$(CN$_6$)$^{(3-)\bullet}$] is rapidly changing with T when approaching the transition temperature. Finally, the softness of the hybrid molecular lattice which allows for the change of dimer conformation (Figure 9) is therefore also an important parameter.

Conclusion

From the point of view of the design, crystal engineering, and chemistry of conducting and magnetic molecular materials, the foregoing results demonstrate the interplay between the sliding motion within one out of three (EDT-TTF-CONH$_2$)$_2$ dimers, coupled to the [Re$_6$Se$_8$(CN$_6$)$^{(3-)\bullet}$]/[Re$_6$Se$_8$(CN$_6$)$^{4-}$] proportion at any temperature, and the electronic ground state of the organic−inorganic hybrid material. In this context, it may be interesting to prevent the metal−insulator and structural phase transitions from occurring and stabilize the Kagome topology (i.e., the high-temperature rhombohedral phase) down to very low temperatures, perhaps by enhancing the electron entropy by increasing the bandwidth or manipulating the band filling[49] by introducing a controlled, larger, yet small number of isostructural and isoelectronic 3^- cluster anions, such as [Re$_5$OsSe$_8$(CN)$_6$]$^{3-}$.[50]

A rich low-dimensional physics emerges from the integrated ESR, static susceptibility, dc conductivity, and ^{1}H spin−lattice relaxation studies of this novel compound, as it has provided a new system among 2D organic conductors in which a structural transition is accompanied by a Mott localization below ca. 200 K. What makes the Mott localization of [EDT-TTF-CONH$_2$]$_6$[Re$_6$Se$_8$(CN)$_6$] so unique is the coupling between the metal−insulator transition and a structural transition allowing the lifting of a degeneracy due to a ternary axis in the high-temperature, strongly correlated metallic phase leading, in turn, to Heisenberg chains at low temperature.

Furthermore the sequence bad metal → paramagnetic insulator→ antiferromagnetic correlations is quite similar to the behavior of κ-(ET)$_2$Cu[N(CN)$_2$]Cl in the pressure regime $P \leq 300$ bar.[48,51] Hence, we can anticipate a strong sensitivity of the Mott localization under pressure, an issue of great relevance

---

(46) See ref 24 as well as (a) Seo, H.; Fukuyama, H. *Synth. Met.* **2003**, *133−134*, 257. (b) Seo, H.; Hotta, C.; Fukuyama, H. *Chem. Rev.* **2004**, *104*, 5005. (c) Miyagama, K.; Kawamoto, A.; Kanoda, K. *Phys. Rev.* **2000**, *B62*, R7679.

(47) Kanoda, K. *Physica C* **1997**, *282−287*, 299.

(48) Lefebvre, S.; Wzietek, P.; Brown, S.; Bourbonnais, C.; Jérome, D.; Mézière, C.; Fourmigué, M., Batail, P. *Phys. Rev. Lett* **2000**, *85*, 5420.

(49) Mori, T. *Chem. Rev.* **2004**, *104*, 4947.

(50) Tulsky, E. G.; Crawford, N. R. M.; Baudron, S. A.; Batail, P.; Long, J. R. *J. Am. Chem. Soc.* **2003**, *125*, 15543.

(51) Limelette, P.; Wzietek, P.; Florens, S.; Georges, A.; Costi, T. A.; Pasquier, C.; Jérome, D.; Mézière, C.; Batail, P. *Phys. Rev. Lett.* **2003**, *91*, 16401.

to the problem of long-range intermolecular electron transfer in the solid state.[21,23,46−48] Note also that the in-plane conductivity of the high-temperature conducting phase is rather low (in between 8 and 3 $(\Omega\ \mathrm{cm})^{-1}$) which again is reminiscent of the bad metal picture which has been proposed for κ-$(\mathrm{ET})_2\mathrm{Cu}[\mathrm{N(CN)}_2]\mathrm{Cl}$ under a pressure of 400 bar, where strong electron correlations decrease significantly the mobility of the carriers in the conducting state.[51]

Finally, we note in closing that it seems that it is the structural transition with a symmetry change which is driving the onset of an insulating state at low temperature in $[\mathrm{EDT\text{-}TTF\text{-}CONH}_2]_6[\mathrm{Re}_6\mathrm{Se}_8(\mathrm{CN})_6]$. The half-filled band 1D chains which form below the transition are insulating (Heisenberg chains) because of the dominance of electron−electron repulsion over the bandwidth. Therefore, the whole study is in favor of the presence of a Mott localization but not of a Mott transition "stricto sensu" as observed instead in other compounds such as κ-$(\mathrm{ET})_2\mathrm{X}$ or vanadium sesquioxide.[52]

Acknowledgment. We thank the CNRS, the Région des Pays de la Loire and the Région d'Aquitaine for support. We also thank Jean-Charles Ricquier for his help in preparing the illustrations. R.M. acknowledges the European Community for support within the framework of the Marie Curie Training Fellowship HPMT-CT-2000-00042. Work at Bellaterra was supported by DGI-Spain (Project BFM2003-03372-C03) and Generalitat de Catalunya (Project 2001 SGR 333). This work was partially supported by the "A. de Betancourt-J. R. Perronet" 2002 Prize of the Spanish Minister of Education awarded to P.B.

Supporting Information Available: Two crystallographic information files (CIF), one Table with crystallographic data, one figure exemplifying the contact configurations for dc conductivity measurements and photographs of high- and low-temperature Bragg reflections. This material is available free of charge via the Internet at http://pubs.acs.org.

JA0523385

---

(52) Limelette, P.; Georges, A.; Jérome, D.; Wzietek, P.; Metcalf, P.; Honig, J. M. *Science* **2003**, 302.